Investigating Dispersive H_2 and CO_2 Transport by means of medical-CT and GC-Supported Core Flooding Experiments

Gerald Stiedl[1,*], *Boris* Jammernegg[1], and *Holger* Ott[1]

[1]Montanuniversity Leoben, Department Geoenergy, 8700 Leoben, Austria

Abstract. This study aims to quantify diffusion and dispersion effects that are important for reactive transport processes and the efficiency of geological hydrogen storage. The focus is on hydrogen storage and hydrogen methanation in formations such as depleted natural gas reservoirs and aquifers. The interactions between the initially equilibrated subsurface system and the injected gases, such as hydrogen or carbon dioxide, are studied experimentally at the macroscopic level using computed tomography-based core flooding. The experiments were carried out in a core flooding facility specially developed to characterise reactive transport processes in porous rock samples under reservoir conditions. Phenomena such as molecular diffusion, dispersion, solubility in the remaining aqueous phase and biochemical reactions influence the purity of the injected components and lead to concentration gradients in reservoirs and geological storage sites. The spatial distribution of fluids and their effect on transport processes has a strong influence on the loss of recoverable hydrogen, as well as on microbial metabolism and, thus, on the growth of biomass in the pore space. This work includes gas-gas dispersion experiments in dry sandstone core samples to quantify diffusive and dispersive effects during gas-gas displacement. Furthermore, comparable experiments were carried out in water-saturated cores to determine the influence of the brine phase usually present in reservoirs and its interaction with the injected gaseous components. The combined data from chemical in-line analysis (gas chromatography) of the effluent gas, in-situ saturation measurements using computed tomography, density and differential pressure measurements will ultimately be used to calibrate reactive transport models that can also be upscaled to the field scale. As a future follow-up to this work, core flooding experiments are planned with core samples that have been incubated with methanogenic microorganisms.

1 Introduction

The growing demand for sustainable energy storage solutions has led to significant interest in underground hydrogen storage (UHS). UHS is a promising solution for large-scale storage of renewable energy in the form of hydrogen gas as a chemical energy carrier. With high and variable storage and withdrawal rates, UHS can align the fluctuating character of renewable energy sources, whereby their full potential can be utilized. This technology can provide the vast storage capacity needed to build a hydrogen infrastructure and achieve the European Union's net-zero greenhouse gas emissions target.

Beside simulations and small-scale trials, the first field tests have been carried out to address and minimize the various uncertainties associated with this new technology. In addition to the safety of such operations, the quantification and purity of the recoverable hydrogen have been elaborated, thereby defining the economic limits and possibilities [1], [2]. Besides technical limitations, storage efficiency primarily depends on the interactions between the injected hydrogen gas and the initially equilibrated subsurface system. On the one hand, natural diffusive and advective processes lead to an unavoidable reduction of recoverable hydrogen. But beyond that, geochemical and biochemical reactions can occur to an uncertain extent, also resulting in a loss of hydrogen and, hence, a loss of stored energy [3]. These processes have to be fundamentally investigated to frame the potential of UHS.

First field-scale operations in depleted natural gas reservoirs have shown that primarily biochemical reactions induced by methanogenic archaea lead to a decline of the stored hydrogen [4], [5]. The metabolism of these microorganisms, which are residing in the pore space of the reservoir rock, converts H_2 together with CO_2 as a carbon source into methane and water according to the so-called Sabatier reaction:

$$4H_2 + CO_2 \rightarrow CH_4 + 2H_2O \qquad (1)$$

* Corresponding author: gerald.stiedl@unileoben.ac.at

This, in terms of hydrogen storage efficiency detrimental impact, yields a new approach to efficiently store excess renewable energy in the form of "renewable" methane. Such operations include a (possibly cyclical) usage of CO_2 and can, therefore, be treated as CCU projects (Carbon Capture and Utilization).

The anaerobic bio-methanogenesis is controlled by the concentration of available substrates, salinity, pressure and the presence of competing microorganisms in the formation water [6]. In-situ gas conversion will, however, result in the formation of biomass in the pore space of reservoir rocks, which may compromise storage capacity and injectivity [7], [8]. The efficiency of the gas conversion predominantly depends on the consortium of the methanogenic archaea and their productivity. To evaluate the performance of such subsurface bio-reactive systems, aspects that control microbial metabolism must be characterized. A sufficient nutrient supply in the form of the injected gas is essential for the bioreaction driven by the microbial population, which is residing in the aqueous phase within the pore space. The concentration of nutrients in the gas phase, however, is determined by diffusive and dispersive processes during displacement, which is the subject of this paper.

The displacement of the gas initially in place by the invading gas stream is subject to dissipation, i.e. the irreversible contribution of the displacement, which will lead to mixing and spreading of the involved gaseous components. This process is called hydrodynamic dispersion and will lead to temporal and local variations of the gas composition. Hydrodynamic dispersion is commonly described with the so-called advection-dispersion equation (ADE), derived from the principle of mass conservation. The ADE for one-dimensional flow can be written as follows [9, 10]:

$$\frac{\partial C}{\partial t} = D(x,t)\frac{\partial^2 C}{\partial x^2} - u(x,t)\frac{\partial C}{\partial x} \qquad (2)$$

where C is the solute concentration, t is time, D is the dispersion coefficient, x is distance, and u is the average fluid velocity. The mass transport and the associated change in concentration can be separated into a random movement according to molecular diffusion and an advective motion in the flow direction. Whereas diffusion alone can be considered independent of the flow rate, mechanical dispersion occurs due to varying fluid velocities in the pore network and depends on the interstitial velocity. An aqueous phase is usually present not only in saline aquifers but also in depleted gas fields, which are considered as potential storage sites for hydrogen. Since the solubility of the individual gas components in the brine phase depends on their partial pressure and, subsequently, on their concentration in the gas phase, the hydrodynamic dispersion will also determine the quantity of dissolved gas components. The dissolved nutrients in the liquid phase must then be transported to the place where the microbes reside. The efficiency of substrate transport in the liquid phase depends on the average distance between the gas/liquid interface and biomass accumulations, and on the main transport mechanism (advective or diffusive dominated). The core flooding set-up introduced in this work was designed and constructed with the aim of evaluating such multi-component systems with mass transfer between the phases and biochemical reactions on a macroscopic scale.

To systematically analyse this complex problem, dry gas-gas displacement tests were carried out in the first step. On the one hand, these are intended to demonstrate the capabilities of the experimental setup and, on the other hand, to serve as a basis for subsequent experiments with increased complexity. With the introduction of a stationary water phase, its influence can be compared with the dry base case. The focus here is on the change in the dispersion behaviour of the gases involved. Not only when a shift in the breakthrough curve is observed but also when there is a deviation in the shape of the dispersion curve, which represents a deviation in dispersivity.

2 Experimental setup and data acquisition

The custom-designed core flooding setup is schematically displayed in **Fig. 1**. Within the core holder, cylindrical rock samples with a length of up to 100 cm and a diameter of 1.5 or 3 inches can be mounted. The core holder is horizontally positioned in a medical CT scanner. To ensure the transmission of X-rays with simultaneous mechanical and thermal stability up to 250 bar and 100 °C, the body of the core holder is manufactured out of PEEK (polyether ether ketone).

The sample is placed in a Viton sleeve under confinement pressure. The confinement fluid surrounding the sealing sleeve is pressurized by an automated cycling pump. The confinement fluid is heated, and the circulation allows the core sample to be continuously maintained at the desired experimental temperature with an accuracy of $\pm$ 1 °C. To force the working fluids through the core sample and to prevent bypassing, the confinement pressure was set 50 bar above the working pressure at any time.

Injection and production of fluids into and from the rock sample is realized through flanges located on the abutting face of the cylindrical core. Liquids and supercritical fluids are injected via high-pressure metering pumps (Vindum Engineering) with constant flow rate or at constant pressure. Gaseous components are injected with defined flow rates via calibrated thermal mass flow controllers (Bronkhorst EL-FLOW series). At the outlet side, a back-pressure system is mounted to adjust the pore

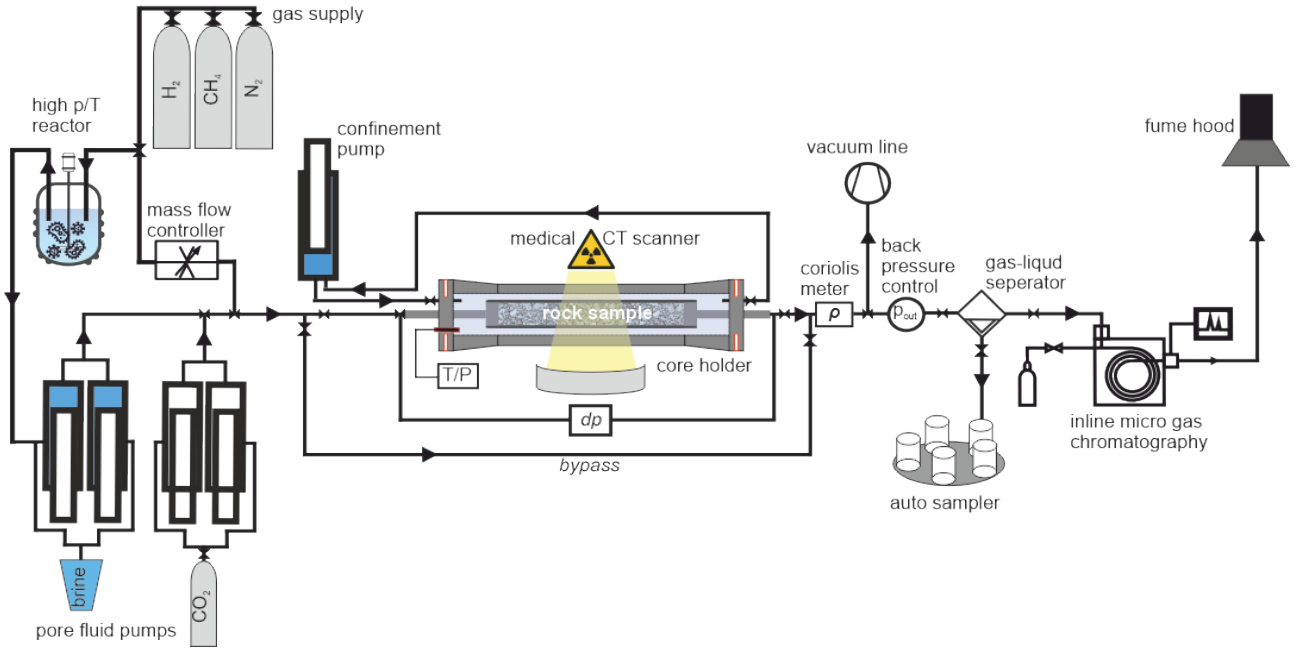

Fig. 1. Schematic of the experimental core flooding setup with the core holder unit, medical CT-scanner, and confinement loop; inlet side (left): metering pumps for injection of liquids and microbial suspensions (grown in high p/T reactor), thermal mass flow controller for gas injection; outlet side (right): inline Coriolis meter, backpressure system, and micro GC.

pressure in the core. The accuracy of the diaphragm-controlled pressure regulator is within 1 - 2 % under the experimental conditions and flow rates. the detailed performance curve can be found in [11]. The operational limit of the core holder design is, depending on sample diameter and temperature, up to 150 bar working pressure. Absolute pressure measurements at the inlet and outlet tubes, as well as a differential pressure measurement via a pressure transducer, enable the monitoring of the hydraulic properties of the system during the experiments. Additionally, a Coriolis meter (Bronkhorst mini CORI-FLOW series) is installed to log the density of the effluent stream, which gives information about the current chemical or phase composition of the produced fluid.

After the pressure relief at the outlet, the gas and liquid phases are separated. Produced liquids can be frequently sampled for further analysis. The gas stream is directly fed into an inline micro gas chromatography system (Agilent 990 Micro GC system) for time-resolved chemical analysis of the effluent gas. The core holder unit is placed and aligned on the movable table of a medical computed tomography scanner (**Fig. 2**). With an adequate scanning interval, the saturation and thus, the phase distributions during the displacement process can be acquired in situ. With a standard medical resolution of 300 µm in the x/y plane and 600 µm along the z-axis, the entire core can be displayed. The CT scanner was operated in single-energy mode with an acceleration voltage of 120 kV.

Fig. 2. Image of the core flooding setup placed on the CT scanner table.

The basic quantity measured by a CT-scanner is the attenuation of X-rays according to Beer's law [12]. Since the linear attenuation coefficient is a function of the electron density and hence the atomic number (Z), it is feasible to identify different fluids (e.g., brine and hydrogen) in a porous rock matrix. Hence, performing differential scans makes it possible to measure 3D porosity map of rock sample, the spatially and time-resolved fluid phase saturations $S_{A,B}$, and dispersive mixing processes. The image reconstruction of the CT-scanner converts the attenuation coefficients µ of each pixel into numerical values, so-called CT numbers. These numbers are normalized to the attenuation coefficient of water. Their unit is called Houndsfield units (HU). To evaluate the saturation of fluid A displacing fluid B at a given time (**Eq. 3**), in addition to the actual scan (CT^{i}_{Core}), reference scans of the core fully saturated ($S_{\alpha} = 1$) with the displacing fluid $\alpha = A$ ($CT^{A,sat}_{Core}$), and with the displaced fluid $\alpha = B$ ($CT^{B,sat}_{Core}$) are required. The time

dependent saturation maps can then be calculated as follows [13, 14]:

$$S_A^i(\vec{x},t) = \frac{CT_{Core}^{Bsat}(\vec{x}) - CT_{Core}^{i}(\vec{x},t)}{CT_{Core}^{Bsat}(\vec{x}) - CT_{Core}^{Asat}(\vec{x})} \qquad (3)$$

In the case of miscible displacement, e.g., between two gases, concentration profiles can be measured instead of phase saturations if the density difference is sufficiently large. With an appropriate scanning interval, concentration profiles over time and the length of the core sample can be recorded. **Fig. 3** shows a 1D concentration profile and a 3D concentration distribution, visualized as 2D colour map during a displacement experiment in a 3-inch dry Berea sandstone core. Supercritical carbon dioxide was displaced by hydrogen gas with a constant injection rate of 100 ml(N)/min (i.e. injected flow rate calculated at standard conditions) in this test run. The scan interval was set to 20 minutes with a scanning time of 11.4 seconds for each scan.

On the upper right panel of **Fig. 3**, the core is visualised at three indicated timesteps. Scan A was taken after 20 minutes of injection, B after 60 minutes, and C at an injection duration of 140 minutes. Gravity overrun due to the lower density of hydrogen compared to carbon dioxide is recognisable in scan B. Because of the complete miscibility of gases, no phase boundaries or defined flow paths can be identified.

On the lower left side, the hydrogen concentration measured with the micro-GC, and the same information evaluated from the CT concentration profiles at the outlet (indicated with the dashed line) is plotted. The gas density, measured with the Coriolis meter at experimental conditions, is also overlaid on the secondary y-axis. The shift in the density curve is recognisable in all H_2-CO_2 displacement experiments and is caused by the initial supercritical state of CO_2 in place, which collapses through the injection of H_2. By diluting the pure CO_2 with the injected hydrogen, the supercritical state cannot be maintained, and the unusual properties associated with it, such as the liquid-like density, cannot be preserved. In the H_2-N_2 test runs, the density decrease was found to be

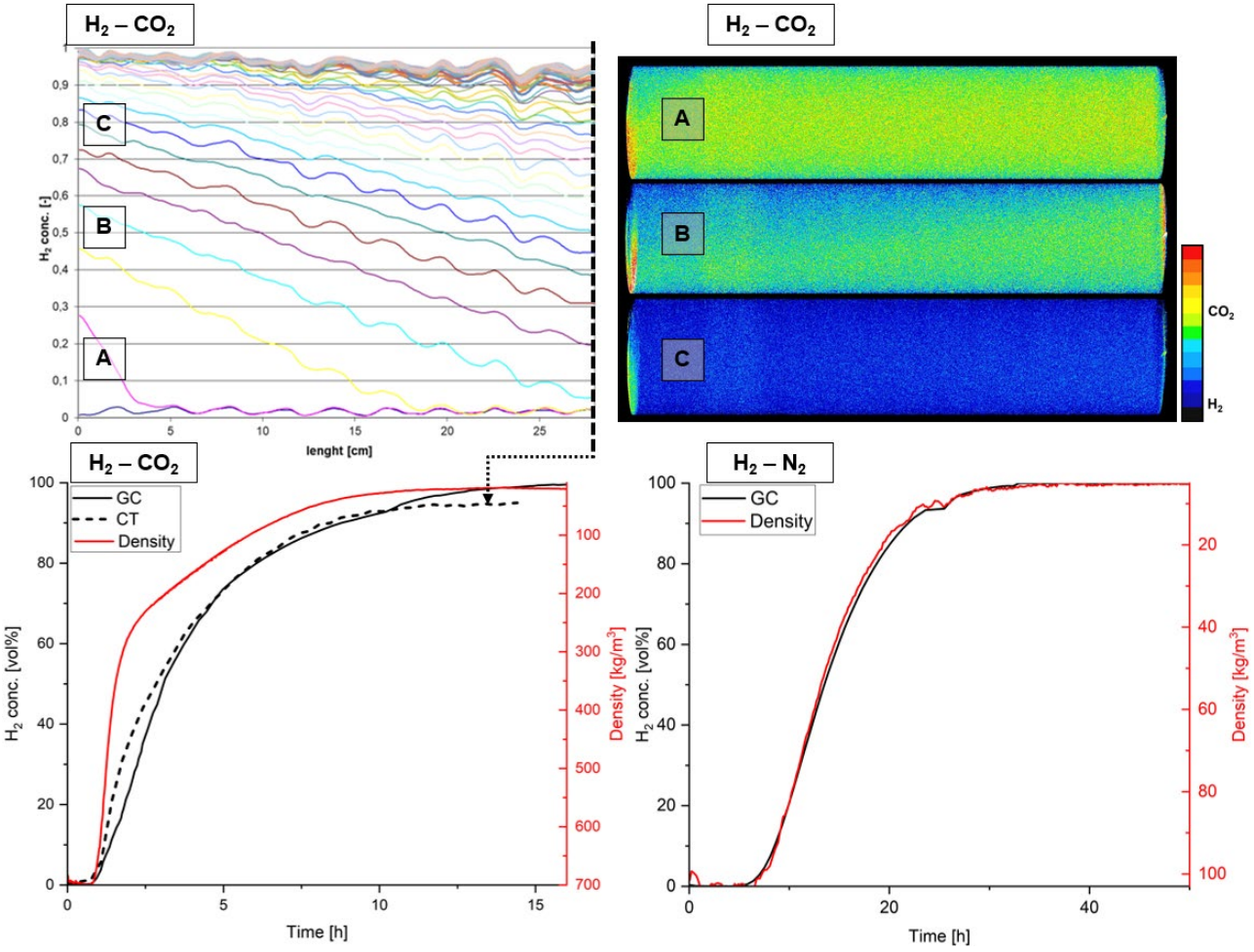

Fig. 3. Upper left: One-dimensional concentration plot of hydrogen displacing supercritical carbon dioxide in a 3 inch × 30 cm long Barea sandstone core, scan interval = 20 minutes; upper right: Visualisation of the core sample at three indicated timesteps; lower left: Hydrogen concentration measured with GC and CT-scanner, and gas density at the outlet; lower right: Hydrogen concentration measured with GC and gas density at the outlet for a H_2-N_2 displacement experiment.

highly consistent with the H_2 concentration from the GC measurements (**Fig. 3** lower right diagram).

With the installed inline micro-GC unit, an accuracy of retention time standard deviation (RSD) of less than 0.25% can be achieved for qualitative determination and quantitative analysis, with a response RSD of less than 1% [15]. The in-situ density measurement accuracy using the Coriolis flow meter has a relative deviation of ± 0.5% [16]. Regarding medical CT scanner measurements, Vinegar and Wellington [17] characterised the sensitivity to saturation changes in multiphase flow experiments using single- and dual-energy modes. With a measurement accuracy of ± 1 HU, changes in saturation could be identified with an accuracy of ± 1% in single-energy scanning operations. As the scanner used in this study has a comparable measurement accuracy, and as the concentrations and saturations are calculated according to the same principle, it can be assumed that the accuracy is in the same range. For medical applications, the manufacturer specifies a practical tissue distinguishability of 3 HU [18]. This corresponds to an absolute saturation accuracy of 3% in this case.

3 Results and interpretation

3.1 Dry gas-gas dispersion

To decompose the bioreactive transport system, a series of experiments with increasing complexity are conducted. With a focus on diffusive and dispersive effects alone, core flooding experiments in dry rock samples were carried out. For this base case scenario, four experiments were carried out on a 1.5-inch core and three experiments on a 3-inch core. The injection rates were set differently for each experiment. The rock samples were fully saturated with nitrogen (gaseous), respectively carbon dioxide (in supercritical state), and subsequently displaced with pure hydrogen gas at a constant flow rate. To quantify the contribution of mixing behaviour, dispersion curves were measured and quantified by fitting an analytical solution for the one-dimensional ADE (**Eq. 2**). According to **Eq. 4**, the resulting dispersion coefficient can be split into a flow rate-independent diffusion term, and a term representing advective dispersion [19]:

$$D = D_m \tau + \alpha u \qquad (4)$$

Where D_m is the binary molecular diffusion coefficient, τ is the tortuosity factor, a dimensionless factor between 0 and 1 and inversely proportional to the tortuosity of the system, u is the flow velocity of the gas, and α is the longitudinal dispersivity, a measure of the heterogeneity of the porous media [19]. Diffusion is not only affected by the porosity ϕ and the tortuosity (expressed as tortuosity factor (τ); in the case of multiphase flow, the corresponding gas saturation S_g) reduces the cross section and must therefore also be considered. The relationship between the binary diffusion coefficient in the bulk fluid $D_{bulk}^{AB}(p,T)$ and the effective diffusion coefficient in the partially saturated porous medium D_{eff}^{AB} can be described as follows [20]:

$$D_{eff}^{AB} = \phi S_g \tau D_{bulk}^{AB}(p,T) \qquad (5)$$

Fig. 4 (upper diagram) shows experimentally obtained concentration profiles of nitrogen gas displaced by hydrogen in a Berea sandstone core plug with 30 cm length (dashed lines), and the fitted curves (solid lines) for three different flow rates. The time scale in this diagram is represented in dimensionless time, t_D. The dimensionless timescale was normalised for each experiment. Thereby, the breakthrough of the 50% hydrogen concentration threshold was defined as $t_D = 1$. The determined dispersion coefficients for the dry H_2-N_2 system are plotted versus the interstitial velocity (according to **Eq. 4**) in **Fig. 4** (lower diagram).

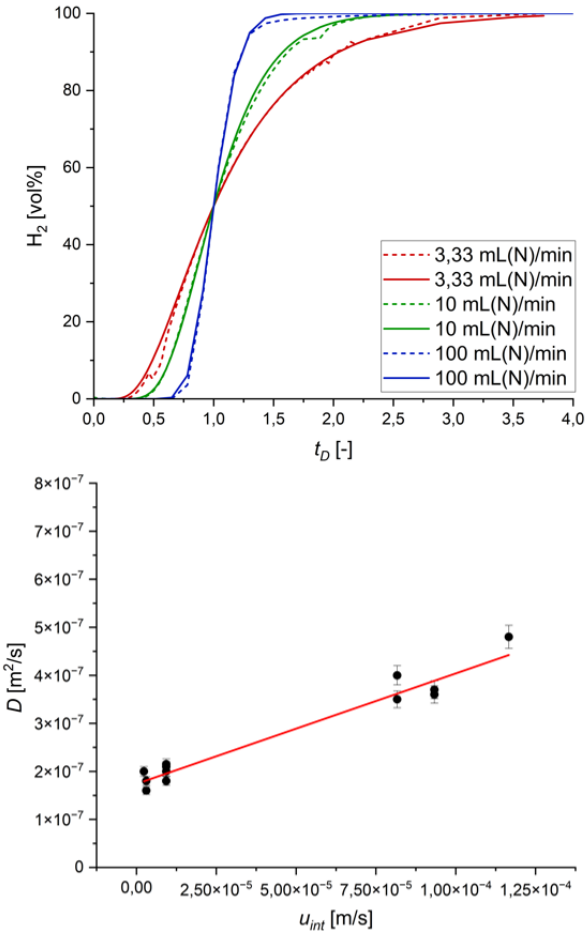

Fig. 4. Upper panel: concentration profiles of hydrogen displacing nitrogen (dashed lines experimental data, solid lines fitted curves) with three different flow rates plotted over dimensionless time; lower panel: dispersion coefficient (D) as a function of the interstitial velocity.

The dimensionless Peclet number (Pe) was calculated for every experiment by multiplying the interstitial velocity u with the characteristic length L, for which we take in the present case, the sample length divided by the dispersion coefficient, $Pe = uL/D_{eff}$. The experiments cover a

range of Peclet numbers from $Pe = 5$ to 78, which indicates that advection dominates the displacement over the acting dissipative mechanisms. The relative weight of diffusion and dispersion contributing to dissipation will be discussed in the following.

With the linear relation in **Eq. 4**, the effective diffusion coefficient D_{eff}^{H2N2} was determined with $1.75 \cdot 10^{-7}$ m²/s. Chen and Othmer [21] reviewed different correlations for calculating gas diffusion coefficients and provided a generalised equation for gas-gas diffusion coefficients, given in cm²/s:

$$D_{1,2} = \frac{0.43 \left(\frac{T}{100}\right)^{1.81} \left(\frac{1}{M_1} + \frac{1}{M_2}\right)^{0.5}}{P \left(\frac{T_{C1}\, T_{C2}}{10000}\right)^{0.1405} \left[\left(\frac{V_{C1}}{100}\right)^{0,4} + \left(\frac{V_{C2}}{100}\right)^{0.4}\right]^2} \quad (6)$$

with T in Kelvin and P in atm being the experimental temperature and pressure, T_C the critical temperature in Kelvin, M the molar weight and V_C the molar volume at the critical point. With this correlation, the bulk diffusion coefficient at our experimental conditions of 100 bar and 50 °C was calculated with $D_{bulk}^{H2N2} = 9.3 \cdot 10^{-7}$ m²/s. By applying **Eq. 5**, the effective diffusion coefficient reduces to $1.55 \cdot 10^{-7}$ m²/s, which is in good agreement with the experimentally obtained value.

3.2 Influence of water saturation

With the introduction of brine into the core samples, the complexity of the reactive system is increased by the presence of an additional phase. Before the actual gas dispersion experiments are started, synthetic brine is injected at initial vacuum conditions until the core is fully brine saturated. Subsequently, the liquid phase is displaced by (sc)CO_2 with a moderate injection rate. The remaining brine is considered as an immobile phase since the gases subsequently injected for the dispersion experiments have a much lower viscosity than the (sc)CO_2, and the gas-brine displacement efficiency is therefore negligible. To determine the remaining brine saturation, the core sample was CT-scanned (**Fig. 5**) before (blue line) and after (red line) the dispersion experiments. The average brine saturation was calculated $S_{brine} = 0.74$; so, the gas saturation (S_g) equalled 0.26, with negligible changes throughout the whole experimental procedure.

The synthetic formation water was chosen in view of our intention to carry out experiments in the future with microbial populations following up on the here presented data. The chemical composition was derived from the microbial active Lehenfeld gas field in Upper Austria [4]. The complete list of ingredients and their concentrations is reported in [22]. For the present experiments without microorganisms, the organic components were omitted, but in order to create comparable conditions with regard to pH value and ion concentrations and thus also gas solubilities, all inorganic components were exactly adopted.

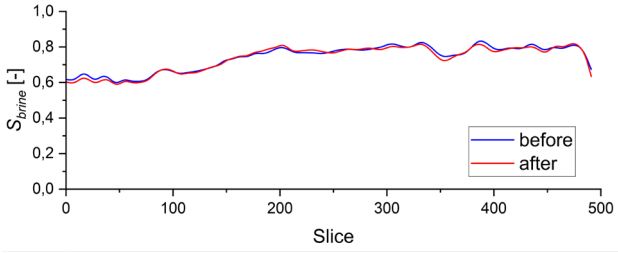

Fig. 5. One-dimensional brine saturation profile before (blue line) and after (red line) a gas dispersion experiment.

According to **Eq. 5**, the new effective Diffusion coefficient for the brine saturated sample was determined to be $D_{eff\ (Sw=0,74)}^{H2N2} = 4.57 \cdot 10^{-8}$ m²/s. The experimentally obtained dispersion coefficients for two different injection rates are plotted against the interstitial velocity in **Fig. 6** (upper diagram). The linear relation indicates the validity of **Eq. 4**, also with the presence of an immobile aqueous phase. Compared to the dry state, a significantly steeper slope, representing the dispersivity (α), has emerged under wet conditions. The distribution of the immobile brine phase introduces an additional level of heterogeneity to the porous medium through which the gas phase travels. Since dispersivity is related to the heterogeneity of the system, the presence of an additional phase occupying parts of the available pore space increases dispersivity. Naveed et al. [23] observed a similar trend in dispersivity during gas dispersion tests conducted at varying water saturation levels. In the experimental framework outlined in this study, dispersivity was found to increase by nearly one order of magnitude, from $2.3 \cdot 10^{-3}$ m to $1.9 \cdot 10^{-2}$ m, when brine saturation reached 0.74, in comparison to the dry test conditions (see **Fig. 6**).

Considering the dispersion behaviour, expressed by the dispersion coefficient, two domains can be distinguished, which are separated by the intersection of the two straight lines in **Fig. 6** (upper diagram). At low flow rates to the left of the intersection, the smaller effective diffusion coefficient D_{eff}^{AB} due to the presence of the water phase, and thus the reduced space available for gas-gas interaction (see **Eq. 5**) is decisive for the lower dispersion in the wet case. At these flow conditions, the additional brine phase leads to an overall less disperse behaviour in the gas phase. At higher interstitial velocities, where advective transport dominates, the elevated dispersivity results in a higher overall dispersion in the wet case compared to the dry pore space.

Fig. 6 (lower panel) shows the hydrogen concentrations of a dry and a water-saturated dispersion test displacing nitrogen with approximately the same interstitial velocities. In the wet scenario, the smearing of the concentration profile is significantly more pronounced compared to the dry test, which is reflected in a smaller Peclet number and a larger dispersion coefficient.

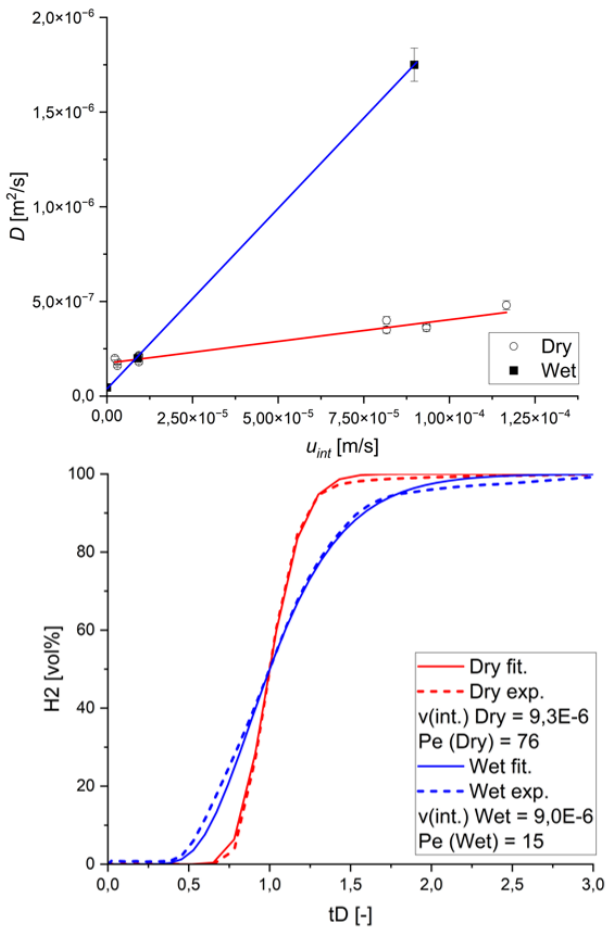

Fig. 6. Upper panel: H_2 dispersion coefficient vs. interstitial velocity for dry and brine saturated ($S_b = 0.74$) conditions; lower panel: Hydrogen concentration profiles of a dry and a water-saturated dispersion experiment displacing nitrogen with similar interstitial velocities.

3.3 Effect of the solubility

The available pore space and its complexity is not the only source of dispersion. Due to the solubility of the gases in the aqueous phase, (a) a retention of relevant gas constituents, and (b), a further smear out of the front can be expected. In order to evaluate the influence of gas solubility on dispersion, the maximum amount of hydrogen that can dissolve in the existing quantity of aqueous phase in the core sample under the prevailing test conditions was calculated. Osman et al. [24] provided hydrogen solubility data at elevated temperature and pressure conditions in pure water and brine. At the test conditions described here, the solubility is in the range of $1 \cdot 10^{-3}$ [mol/mol]. For the 3 inch × 30 cm core plug, considering the porosity and water saturation, this gives a maximum absolute amount of 0.01 moles of hydrogen that can dissolve in the aqueous phase, corresponding to 0.0103 pore volumes (PV).

After injection of 1 PV, a hydrogen concentration of 0.95-0.99 [vol. fraction] was detected at the outlet, depending on the flow rate and the associated dispersive smearing of the concentration profile. As a consequence, the amount of soluble hydrogen is in the range of 1% of the total injected hydrogen and would hardly be detectable in the experiment.

This result indicates that, due to the low solubility of hydrogen, this effect cannot be resolved in the experiment and may not be of practical relevance for the gas stoichiometry in the field. It should be noted that the extreme scenario of the maximum soluble quantity was elaborated here. Due to the exact distribution of the gas and water phases, the expansion of the phase boundaries and the homogeneous distribution of hydrogen in the brine phase, the actual amount of dissolved hydrogen is likely to be less than the calculated amount. However, this picture may change with the introduction of hydrogen-consuming microorganisms.

A more detailed and accurate understanding of the experimental results can be achieved through numerical history matching of the experimental responses. This numerical description can incorporate measured rock heterogeneity in a stochastic manner. History matching also enables the experimental results to be extended numerically to different degrees of heterogeneity and brine saturation distributions. This numerical extension could minimise the experimental effort and investigation time required.

4 Summary and conclusion

This study provides an experimental method for the investigation of reactive transport processes in the subsurface. With the aid of CT- and GC-supported core flooding experiments, diffusive and dispersive effects, which can be decisive for the efficiency of UHS and in situ methanation operations, were characterised on a macroscopic scale. Initial experiments have shown that the extensive data acquisition allows a detailed description of the transport processes taking place in the pore space of a potential storage site.

Through experiments with different injection rates, flow regimes with more diffusive or more advective character in the pore space could be established. Peclet numbers were determined, and a range of more than one order of magnitude could be covered. The experimentally obtained dispersion curves were quantified by fitting an analytical solution. Thus, the dispersion coefficient could be calculated, and through the correlation of the dispersion coefficient with the interstitial velocity, the effective gas-gas diffusion coefficient could be determined. This was compared with a generalised empirical equation for binary gas diffusion coefficients with good agreement.

With the introduction of a brine phase, the influence of an additional, immobile liquid phase on the gas transport could be studied. It was found that at low flow rates, the reduced effective diffusion coefficient compared to the dry case is decisive for the overall lower dispersion behaviour of the system. At higher flow rates, the increase in dispersivity dominates and leads to a more pronounced

smearing of the dispersion curve in the brine-saturated case with the same interstitial velocity compared to the dry system. The increase in dispersivity can be caused by the reduction in available spore space and the additional contribution of tortuosity due to the presence of the additional phase. The exact distribution of the aqueous phase seems to be crucial for advective mixing. For this reason, µCT measurements are planned with rock samples in a dry state and with different water saturations. The tortuosity should be evaluated as a function of the water saturation.

Another fundamental mechanism leading to dispersion is related to the dissolution of gas components in the aqueous phase. Due to different dissolution kinetics and limits, gas components transfer to the brine phase to varying degrees, altering the stoichiometry at the front and increasing dispersion. The influence of hydrogen solubility on dispersion was estimated by comparing the maximum possible hydrogen loss due to solubility with the total amount of hydrogen injected. This maximum hydrogen loss was estimated to be less than one percent of the hydrogen injected, which is below the detection limit of the experimental setup and does not lead to any significant change in the stoichiometry of the produced gas.

Future work will include experiments with active methanogenic microorganisms. One expected effect is an increased mass transfer from the gas phase to the brine phase due to continuous nutrient consumption by the microorganisms. Furthermore, dispersion is likely to be affected by the distribution of the aqueous phase in the pore space and on the macroscopic scale. The growing biomass binds water and eventually modifies the brine distribution in the rock, thus influencing the gas dispersity.

In addition to the experimental work, simulations will be used to numerically history-match the experimental data and to characterise the influence of the degree of heterogeneity of the rock and the water phase.

References

1. D. Zivar, S. Kumar, and J. Foroozesh, Int. J. Hydrogen Energy, **46**, 23436-23462, (2021)
2. R. Tarkowski, Renewable and Sustainable Energy Reviews, **105**, 86-94, (2019)
3. R. Tarkowski and B. Uliasz-Misiak, Renewable and Sustainable Energy Reviews, **162**, 112451, (2022)
4. M. Pichler, H. Konegger, A. Loibner, and S. Bauer, "Final Report: Underground Sun Conversion," RAG Austria AG, Austria, (2021)
5. P. Šmigáň, M. Greksák, J. Kozánková, F. Buzek, V. Onderka, and I. Wolf, FEMS Microbiol. Lett., **73**, 221-224, (1990)
6. K. Coyte, H. Tabuteau, E. Gaffney, K. Foster, and W. Durham, Proc. Natl. Acad. Sci. USA, **114**, (2016)
7. N. Hassannayebi, S. Azizmohammadi, M. De Lucia, and H. Ott, Environ. Earth. Sci., **78**, (2019)
8. E. M. Thaysen, S. McMahon, G. Strobel, I. Butler, B Ngwenya, N. Heinemann, M. Wilkinson, A. Hassanpouryouzband, C. McDermott, K. Edlmann, Renewable and Sustainable Energy Reviews, **151**, 111481, (2021)
9. J. Delgado, Heat and Mass Transfer, **42**, 279-310, (2006)
10. A. Kumar, D. K. Jaiswal, and N. Kumar, J. Hydrol., **380**, 330-337, (2010)
11. Equilibar, LLC, Equilibar Research Series Back Pressure Regulators, 2025. Accessed: Jun. 17, 2025. [Online]
12. S. Akin and A. R. Kovscek, Geological Society, London, Special Publications, **215**, 23-38, (2003)
13. X. Miao, Y. Wang, L. Zhang, N. Wei, and X. Li, Micron, **124**, 102703, (2019)
14. H. Ott, S. Oedai, Geophys. Res. Lett., **42**, 2270-2276, (2015)
15. J. Zhang, Application Note: "Analysis of Fischer-Tropsch Syngas and Tail Gas with the Agilent 990 Micro GC," Agilent Technologies, (2023)
16. Bronkhorst High-Tech B.V., Datasheet: Mass Flow Meter/Controller for Gases – EL-FLOW Prestige [3155-M12-EN], Accessed: Jun. 18, 2025. [Online]
17. H. Vinegar, S. Wellington, Rev. Sci. Instrum. **58**, 96-107 (1987)
18. Siemens Healthineers, Official Website. Accessed: Jun. 17, 2025. [Online]
19. M. S. Costanza-Robinson and M. L. Brusseau, *Gas Transport in Porous Media*, (Springer Netherlands, C. K. Ho and S. W. Webb, 2006).
20. J. Michelsen, N. Langanke, B. Hagemann, S. Hogeweg, and L. Ganzer, *Advanced SCAL for Carbon Storage & CO_2 Utilization*, SCA2023-032, (2023).
21. N. H. Chen and D. F. Othmer, J Chem Eng Data, **7**, 37-41, (1962)
22. P. Jasek, H. Konegger, A. P. Liobner, and H. Ott, "Alteration of hydraulic rock properties during subsurface hydrogen methanation," (2025). (to be published)
23. M. Naveed, S. Hamamoto, K. Kawamoto, T. Sakaki, M. Takahashi, T. Komatsu, M Wollesen de Jonge, M Lamande, P. Moldrup, Soil Science Society of America Journal, **76**, 845-852, (2012)
24. A. Osman, N. Mehta, A Elgarahy, M. Hefny, A. Al-Hinai, A. Al-Muhtaseb, D. Rooney, Environ. Chem. Lett., **20,** (2021)